



Design, establishment, analysis, and quality control of a high-precision reference frame in Cortes de Pallás (Spain)

Luis García-Asenjo¹ · Laura Martínez² · Sergio Baselga¹ · Pascual Garrigues¹ · Raquel Luján¹

Received: 1 December 2022 / Accepted: 6 December 2022 / Published online: 15 February 2023
© The Author(s) 2023

Abstract

A high-precision geodetic reference frame was required in Cortes de Pallás (Spain) to undertake a long-term deformation monitoring project. Involving distances up to 2000 m, the aimed accuracy was 1 mm and 3 mm for horizontal and vertical components, respectively. Such a high precision is necessary to detect possible displacements of selected points on a critical rocky area in a short period of time, i.e., 2 or 3 years, and also to provide ground control for the integration of precise 3D models periodically obtained by remote sensing techniques. Considering the historical geotechnical problems of the area, the possible influence of the hydroelectric power plant, and the peculiar orography of the zone, a proper analysis of the stability is crucial if the reference frame is to be used for rigorous over-time deformation monitoring. This paper describes the deformation monitoring of a 10-pillar geodetic network which was measured from 2018 to 2020 by using a sub-millimetric Mekometer ME5000 (0.2 mm + 0.2 ppm) along with a demanding observing methodology which includes a network of data loggers for temperature, humidity, and air pressure as well as proper calibration of sensors and instruments to prevent potential inconsistencies between the scale of the network and the unit of length of the International System (SI meter). The results demonstrated that the chosen methodology yielded the aimed accuracy. However, using such a high precision methodology entails the problem that small displacements of only 1 or 2 mm are significantly detected as deformations by conventional deformation analysis and then it arises the problem of finding a subset of stable points for a rigorous datum realization when all the points seem to displace. This general problem is analyzed in the particular case of Cortes de Pallás, where a balanced mix of deformation analysis and technical decisions was eventually adopted to define a precise and stable reference frame for rigorous over-time deformation monitoring.

Keywords Geodetic network · Reference frames · Deformation monitoring · Sub-millimetric EDM · ME5000 · Length metrology

Introduction

A high-precision 3D reference frame was set up as a basic component of a long-term deformation monitoring in Cortes de Pallás (Spain). To detect possible displacements of huge boulders in a short period of time, e.g., 2 or 3 years, the accuracy requirement for this reference frame was deemed to be around 1 mm and 3 mm for horizontal and vertical components, respectively. This reference frame is also used

to provide ground control to remote sensing techniques such as terrestrial digital photogrammetry (TDP) or terrestrial laser scanning (TLS) (Di Stefano et al. 2020; Harmening and Neuner 2019).

However, this 3D reference frame has to face four challenges. First, the harsh orography of the area (Fig. 1), which includes a water reservoir and strong height differences, entails severe limitations in the geodetic network design as well as long distances between pillars (up to 2000 m). Second, such a high precision at those distances (better than 1 ppm) can only be obtained by using very accurate sub-millimetric electronic distance meters (EDM) like the Mekometer ME5000 (Bell 1992; Rüeger 1996) along with a dedicated procedure which includes, among other ingredients, rigorous refraction correction (Rüeger 1996) and length metrology methods (García-Asenjo et al. 2017). Three, sporadic displacements due to the activity

Laura Martínez, Sergio Baselga, Pascual Garrigues, and Raquel Luján contributed equally to this work.

✉ Luis García-Asenjo
lugarcia@cgf.upv.es

Extended author information available on the last page of the article.



Fig. 1 Overview of the electricity power complex in Cortes de Pallás. The four extreme pillars of the geodetic network are sketched in yellow (8001, 8007, 8008, 8010), and the critical area to be monitored is framed in red

of the water pumping system (Fig. 2) could be superposed on slow terrain deformations and one-occurring motions. Four, the reference frame has to prove stable along time. Otherwise, the instability of individual points should be properly determined and considered for subsequent surveys using those points as stations.

Before pillar construction, several alternatives were analyzed for the network to meet economy, precision, and reliability in accordance with the classical approach for optimization problems in geodetic networks (Grafarend and Sansò 1985; Klein et al. 2019). Since a precise vertical control cannot be effectively included because carrying out a levelling traverse to points No.8007 and No.8010 is difficult and time consuming, the frame was carefully designed as a pure 3D trilateration network. The results obtained in years 2018, 2019, and 2020 confirmed that the aimed high accuracy was accomplished for each individual campaign.

However, a proper diagnosis of the network stability becomes crucial if the geodetic network is intended to be used as a reference frame to provide specific check points or ground control for the TDP and TLP techniques. In fact, the quality of these image-based methods as applied to deformation monitoring strongly depends on a proper



Fig. 2 Detail of the La Muela II plant, with the critical area in red and four of the ten pillars in yellow

integration of their 3D models or point clouds into a unique and well-defined reference system (Francioni et al. 2018).

Since optimal strategies and methods for multi-epoch deformation analysis are still under discussion (Niemeier and Velsink 2019; Nowel 2019; Wiśniewski and Zienkiewicz 2016; Velsink 2015), we considered it sensible for a first diagnosis of the network stability to use conventional deformation analysis (CDA) based on the use of descriptive models (Niemeier 1981; Chen 1983; Caspary 1987; Chen et al. 1990) to test three initial hypothesis: (1) all the points are stable under a pure 3D approach, (2) only those points opposite to the critical area on the cliff (8001, 8002, 8008, 8009) are stable under a pure 3D approach, (3) stable points are searched by an iterative 2D+1D CDA process.

Given that no conclusive results could be obtained from the three tested hypothesis, we opted for a solution that combines both CDA and geodetic criteria to determine a valid set of precise coordinates for subsequent use of the network as a reference frame as well as an assessment of the uncertainty of those coordinates.

For the sake of conciseness, only the results for hypothesis (1) and the final solution adopted will be presented and discussed.

Methods

Functional model

The measured slope distances were corrected as described in Section 2 and then adjusted by using the following functional model

$$-\frac{x_j - x_i}{D_{ij}^c} dx_i - \frac{y_j - y_i}{D_{ij}^c} dy_i - \frac{z_j - z_i}{D_{ij}^c} dz_i + \frac{x_j - x_i}{D_{ij}^c} dx_j + \frac{y_j - y_i}{D_{ij}^c} dy_j - \frac{z_j - z_i}{D_{ij}^c} dz_j - (D_{ij}^c - D_{ij}^m) = v_{ij} \tag{1}$$

where,

$D_{ij}^c = \sqrt{(x_j - x_i)^2 + (y_j - y_i)^2 + (z_j - z_i)^2}$ is the computed distance from i to j
 D_{ij}^m is the measured distance from i to j
 (x_i, y_i, z_i) are the local coordinates of i
 (x_j, y_j, z_j) are the local coordinates of j .

The coordinates used in this functional model are referred to the CP2017 local cartesian system which was conventionally defined to facilitate the deformation analysis as well as the processing and integration of image-based techniques. The xz -plane of this local system was placed to be approximately coincident with the area of interest (Table 1).

One advantage of this conventional definition is that the coordinates and precisions obtained from the adjustments can be converted into different coordinate systems of interest with no loss of accuracy. Therefore, the adjusted coordinates for each campaign were available in the following coordinate systems: local CP2017(x, y, z), ETRS89 geodetic (φ, λ), and ETRS89-TM30 (E, N), along with both ellipsoidal h and orthometric H heights, thus covering all technical needs.

Individual free-network solution for each epoch

With equations of the type of Eq. 1, the sample model for epoch i is written in the usual form

$$l_i + v_i = A_i x_i \quad , \quad P_i = Q_i^{-1} \tag{2}$$

where,

l_i vector of m_i distances observed in epoch i
 v_i vector of m_i residuals for epoch i
 $A_i = m_i \times u_i$ configuration matrix for epoch i
 x_i vector of u_i estimated parameters for epoch i
 $P_i = m_i \times m_i$ weight matrix of observations for epoch i .

Table 1 Conventional definition of the CP2017 local system. Geodetic coordinates are referred to the European Terrestrial Reference Frame (ETRS89)

Parameter	Value
x_0	800.0000 m
y_0	800.0000 m
z_0	150.0000 m
φ_0	39° 14' 47.98063"
λ_0	−0° 55' 55.55670"
h_0	520.57344 m
α_0	230.0000 gon

Since distances are the unique type of measurement used and no point can be considered as fixed to estimate the solution for each individual epoch, the system of normal equations

$$N_i = A_i^t P_i A_i \tag{3}$$

has a rank-deficiency $d = 6$. Therefore, the origin and orientation of the network have to be externally defined by providing $c = 6$ constrains (see Section “Approximate coordinates”).

An alternative to overcome this datum defect is the use of the Moore-Penrose pseudoinverse (Blaha 1982), but it would entail that (1) all the points are assumed to be stable and equally valid for the datum definition, and (2) no reduction or extension of the network is admissible over time. Therefore, we opted for the use of a matrix of the datum constraints S (Blaha 1982; Caspary 1987)

$$S^t = \begin{bmatrix} 1 & 0 & 0 & \dots & 1 & 0 & 0 \\ 0 & 1 & 0 & \dots & 0 & 1 & 0 \\ 0 & 0 & 1 & \dots & 0 & 0 & 1 \\ 0 & +\bar{z}_1 & -\bar{y}_1 & \dots & 0 & +\bar{z}_n & -\bar{y}_n \\ -\bar{z}_1 & 0 & +\bar{x}_1 & \dots & -\bar{z}_n & 0 & +\bar{x}_n \\ +\bar{y}_1 & -\bar{x}_1 & 0 & \dots & +\bar{y}_n & -\bar{x}_n & 0 \end{bmatrix} \tag{4}$$

being $(\bar{x}_1, \bar{y}_1, \bar{z}_1, \dots, \bar{x}_n, \bar{y}_n, \bar{z}_n)$ the arrangement of approximate coordinates of the n points assumed to be stable and referred to the center of gravity of the datum

$$\bar{x}_i = x_i - \frac{\sum_1^n x_i}{n}, \quad \bar{y}_i = y_i - \frac{\sum_1^n y_i}{n}, \quad \bar{z}_i = z_i - \frac{\sum_1^n z_i}{n} \tag{5}$$

In order to achieve numerical stability, the matrix S^t is normalized by means of $S_n^t = (S^t S)^{-1/2} S^t$ such that $S_n^t S_n = I$. The adjustment solution for each epoch i is then given by

$$Q_{\hat{x}_i} = (N_i + S_n S_n^t)^{-1} N_i (N_i + S_n S_n^t)^{-1} \tag{6}$$

which is in turn used to compute the vector of estimated parameters \hat{x}_i , the vector of residuals \hat{v}_i , and the variance of unit weight $\hat{\sigma}_{0i}^2$

$$\hat{x}_i = Q_{\hat{x}_i} A_i^t P_i l_i, \quad \hat{v}_i = A_i \hat{x}_i - l_i, \quad \hat{\sigma}_{0i}^2 = \frac{\hat{v}_i^t P_i \hat{v}_i}{f_i} = \frac{\Omega_i}{f_i} \tag{7}$$

with $f_i = m_i - u_i + c =$ degrees of freedom.

Each solution was globally tested to validate the correctness of the model. Subsequently, the outlier detection was performed by using both Baarda’s data snooping and Pope’s Tau method (Lehman and Lösler 2016).

Procedure for testing the coordinate differences

The classical congruency test was the method used to detect possible point displacement between epochs (Niemeier 1981; Caspary 1987). This type of test aims at detecting weather or not the geometry of networks measured at different epochs can be considered statistically identical. Thus, real displacements of points can be distinguished from small displacements caused by the uncertainty of the measurements.

Assuming that two epochs are adjusted with the same datum (S-System), the null hypothesis H_0 of the congruency test is given by

$$H_0 : E(\hat{x}_i) = E(\hat{x}_j) \quad (8)$$

which is equivalent to state that the vector of their coordinate differences \hat{d} is null. The significance difference \hat{d} is tested by the well-known statistic

$$F_d = \frac{\hat{d}^t Q_{dd}^+ \hat{d}}{\hat{\sigma}_0^2 h} = \frac{q_\Delta}{\hat{\sigma}_0^2 h} \quad (9)$$

where,

$$\begin{aligned} \hat{d} &= \hat{x}_j - \hat{x}_i && \text{is the difference vector} \\ Q_{dd} &= Q_{x_i x_i} + Q_{x_j x_j} && \text{is the covariance matrix of the difference vector} \\ h & && \text{rank of the cofactor matrix } Q_{dd} \\ \hat{\sigma}_{0ij}^2 &= (\hat{\sigma}_{0i}^2 + \hat{\sigma}_{0j}^2) / (f_i + f_j) && \text{variance unit of weight of the combined solution.} \end{aligned}$$

The null hypothesis is not rejected with a level of significance α if the ratio F_d follows a Fisher distribution with h and $f = f_i + f_j$ degrees of freedom

$$F_d \leq F_{h, f, \alpha} \quad (10)$$

and the difference vector \hat{d} is considered statistically null. On the contrary, if $F_d > F_{h, f, \alpha}$ the null hypothesis fails and it must be concluded that there has been a significant change in coordinates between epochs.

The investigation of the underlying reasons for that overall network distortion is normally done by using a single point diagnosis which can be approached in different ways. We have used the conventional method that consist in splitting the quadratic form q_Δ in Eq. 9 into as many sub-forms as points contributing to the displacement vector \hat{d} . Each single sub-form expresses the individual contribution of that point to the total form q_Δ and it is 3D tested. Alternatively, the point deformation can be tested by splitting the total 3D displacement into its horizontal (2D) and vertical (1D) components.

Network description

Site and particular aspects

The area to be monitored is a broad cliff (650-m long, 200-m high, and 300-m wide) facing the north side of a flat-topped hill in Cortes de Pallás (Spain). This critical area is located within the Cortes-La Muela hydroelectric power complex, which in turn comprises Cortes II, La Muela I y La Muela II plants.

La Muela II, near to the critical area, consists of four reversible pump turbines which use excess of energy generation capacity to store water in the upper reservoir during nighttime off-peak hours. During peak daylight hours, the accumulated water is dropped with a flow rate of 192 m³/s to the lower reservoir as a conventional hydroelectric facility.

Water flows between the two reservoirs via the underground power station through an 840-m long, 5.45-m diameter, and 45°-inclined penstock housed in a conduction tunnel structure (see Fig. 2). These lifting and dropping operations are suspected to provoke vibrations and possible temporal deformations which may be superimposed on a general and slow geological deformation.

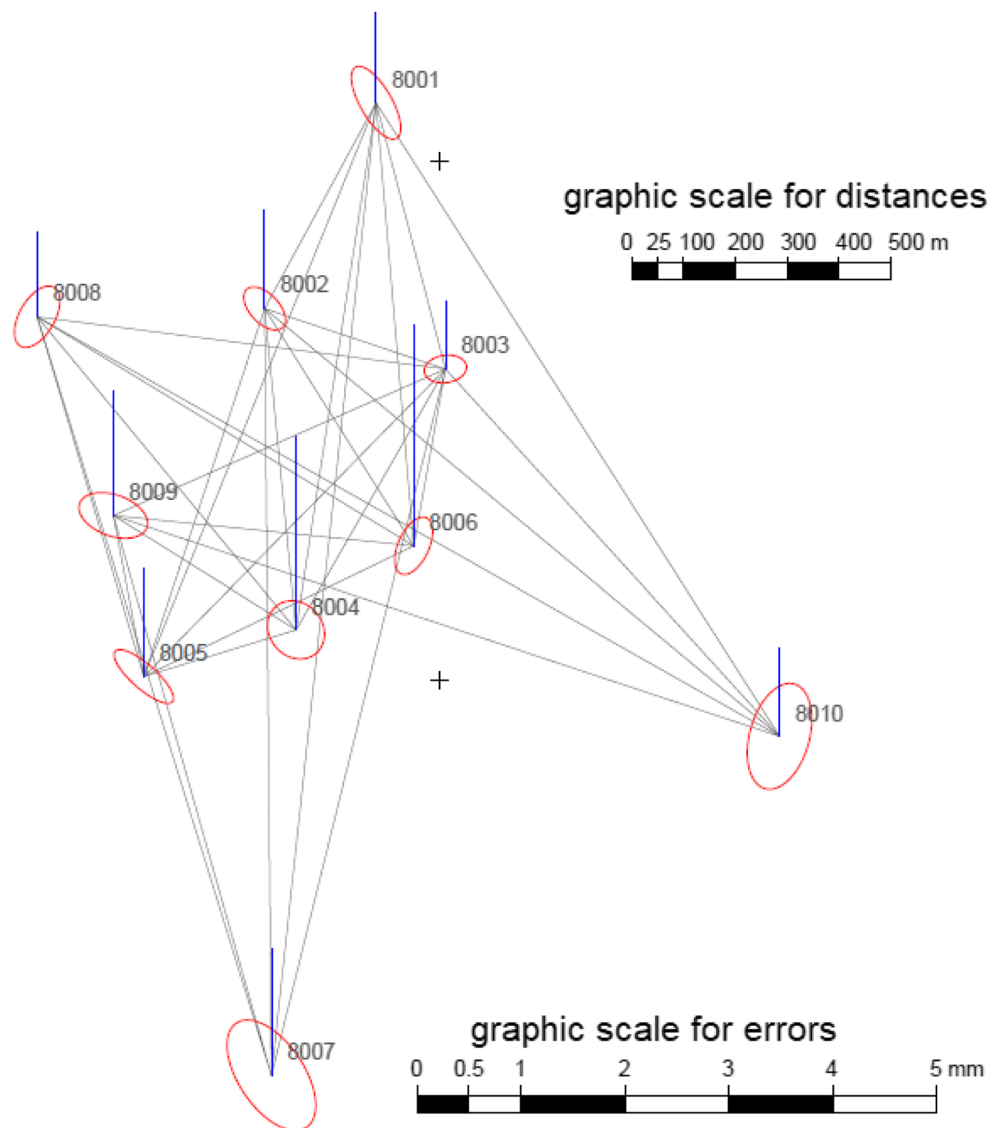
In 2015, the power plant facilities and several roads skirting the cliff were seriously damaged due to a sudden rockfall. Once the refurbishment and consolidation works were finished in late 2017, the Department of Roads and Infrastructures of the *Diputació de València* and the *Universitat Politècnica de València* (UPV) started a 3-year project to monitor both the installed anchoring systems as well as the entire cliff.

Geodetic network

A basic component of the monitoring project is a ten-pillar geodetic network (Fig. 3) whose stability is periodically monitored by using sub-millimetric EDM techniques (García-Asenjo et al. 2019). Eight of these pillars (all except No. 8007 and No. 8010 due to lack of direct visibility) are used periodically as reference stations to monitor a number of reflectors installed permanently within the critical area and to provide ground control for the TDP and TLS campaigns.

However, the area presents serious limitations for any measurement technique. Aside from the usual problems with obstacles or vegetation, there is a water reservoir which strongly limits the selection of optimal stations for both geodetic techniques and image-based techniques. The stations have to be either very close, thus impeding optimal geometries, or they have to be placed on the opposite shoreline involving distances ranging from 400 to 2000 m.

Fig. 3 Free-network solution for year 2019. Standard error ellipses in red and vertical precision in blue



Computing process

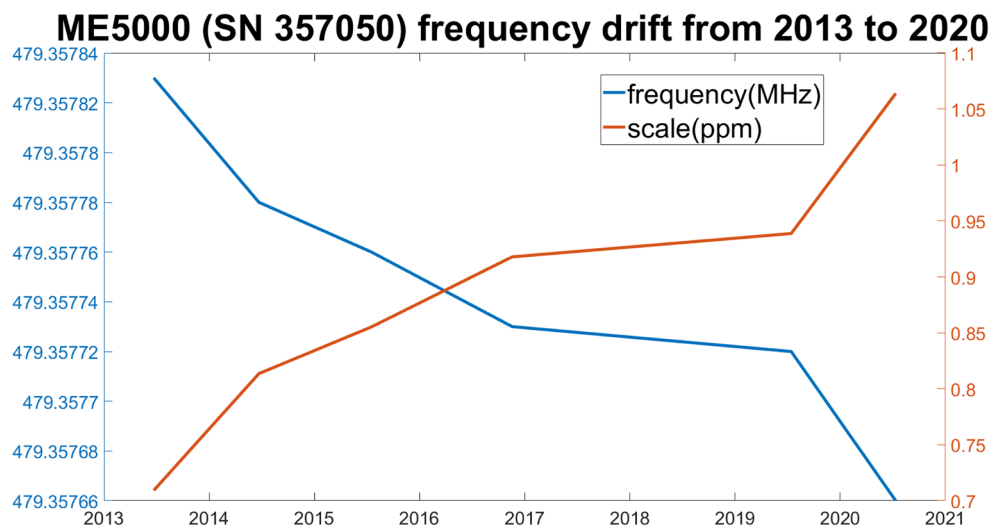
Prior to the adjustment, the following corrections were applied to distances: refraction correction, EDM frequency drift correction, and geometric correction. Some relevant aspects are following explained.

Approximate coordinates

A set of approximate coordinates is required for both the geometrical correction and subsequent adjustment of the measured distances. However, given that the precision of the measured distances is better than 1 mm and the least squares method needs initial coordinates to be known with a relative precision of 10^{-5} so that one iteration suffices, the aimed accuracy for approximate coordinates was 5 mm.

Since only distances are measured, the origin and the orientation of the 3D geodetic network have to be defined by convention. We opted for fixing the official ETRS89 coordinates of the pillar No. 8007 and the ITRF14 (2018.6299) orientation of the baselines 8007-8001 and 8007-8010, which were determined by using 10-h GNSS sessions collected during nighttime in pillars 8001, 8007, and 8010 (see Fig. 1). This initial set of approximate coordinates, which was called CP-FRM00, is also used to check and analyze all the distances for each field campaign. This pre-processing solution is carried out to detect possible problems concerning individual distances, initial coordinates or EDM scale by means of a minimum constrain solution by fixing the coordinates of points No. 8001 and No. 8007, which is the longer line, and the vertical coordinate of No. 8010. For the three pre-processing

Fig. 4 Frequency drift for the used ME5000 as measured in the UPC calibration laboratory from 2013 to 2020



solutions, only eleven residuals showed an absolute value above 1 mm, and only one (2.71 mm) was detected as an outlier.

Refraction correction

For each distance, both the air index *n* and coefficient *K* of refraction were determined at both ends by means of the meteorological parameters. The index of refraction *n* was computed using the expression for the refraction index recommended in the resolution from the General Assembly of the IUGG when the required precision is 10⁻⁷ (IUGG 1999; Ciddor 1996; Ciddor and Hill 1999; Ciddor 2002; Pollinger 2020) and the coefficient of refraction *K* was obtained from the usual expression (Dodson and Zaher 1985; Baselga et al. 2014).

Once the values of *n* and *K* are determined at both ends, the average value is used to compute the first and second velocity corrections as well as the arch-to-chord correction (Bell 1992; Rüeger 1996). As expected, the last two corrections were negligible, but the absolute values obtained for the first velocity correction ranged from 5.81 to 64.74 mm.

EDM frequency correction

The ME5000 (SN 357050) was adjusted in 1989 to realize a nominal carrier frequency of 479.35817 MHz with a scale factor of 0.99999994. However, this scale factor changes with time due to the quartz oscillator ageing (Bell 1992; Rüeger 1996). Therefore, the actual frequency of the EDM has to be determined in a calibration laboratory and the derived scale factor applied subsequently to correct the field distances.

The applied scale factors were 0.918 ppm, 0.939 ppm, and 1.064 ppm for years 2018, 2019, and 2020, respectively. The rapid variation of the EDM frequency observed since 2013 might indicate a potential scale problem (Fig. 4). Unfortunately, the scale cannot be externally validated due to the lack of calibration baselines for distances of several km and nominal distances known with 10⁻⁷ uncertainty. At present, only Nummela Standard Baseline in Finland (Jokela and Häkli 2010) could provide that standard, but its maximum length is limited to 864 m. Hopefully, the novel European standard baseline EURO5000 at the Pieniny Kippen Belt (Poland) will be available in a near future (Pollinger et al. 2021).

Table 2 Summary of the results for the free-network solutions

Year	Ω_i	f_i	$\hat{\sigma}_0^2$	100% \hat{v}_i
2018	5.195	5	0.439	< 0.3 mm
2019	9.457	8	1.182	< 0.6 mm
2020	8.755	8	1.094	< 0.5 mm

Table 3 Congruency test results by applying conventional deformation analysis

Years	$\hat{\sigma}_0^2$	q_Δ	f	h	F_d	$F_{0.95,h,f}$	Def
18–19	0.896	275.48	13	21	14.63	2.44	Yes
19–20	1.138	473.83	16	24	13.64	2.23	Yes
18–20	0.842	1564.62	13	21	69.42	2.44	Yes

Geometric reductions

The measured distances are referred to the center of the instrument and the corresponding reflector. Since their height above pillars are different and vary from one station to other, distances have to be corrected to obtain the distances between the head of pillars. This geometrical correction requires the heights to be accurately measured (better than 1 mm) and good approximate coordinates. The geometric corrections ranged from -2.06 to $+0.6$ mm.

Results

Solution under the hypothesis that all points are stable

Under the hypothesis that no point displaced from 2018 to 2020, the matrix of the datum constrains S^l includes

the coordinates of those points common to the three campaigns. Since point No. 8006 was not observed in 2018, its coordinates were not included and thus, the solution minimizes the trace of the cofactor matrix associated with the remaining 9 points (Tables 2 and 3).

For all the solutions, the average values of the four corrected distances for each baseline were adjusted with a priori error of $0.2 \text{ mm} + 0.2 \text{ ppm}$. All of them succeeded the global test of the model, being the variance of unit weight $\hat{\sigma}_0^2 = 0.439$, $\hat{\sigma}_0^2 = 1.182$, and $\hat{\sigma}_0^2 = 1.094$, respectively. Regarding residuals, 100% were below 0.3 mm, 0.6 mm, and 0.5 mm, respectively (Table 2).

The subsequent single point 3D analysis showed that only points No. 8001, No. 8003, and No. 8010 could be considered stable after 2 years of monitoring. A selection of the deformations obtained under this hypothesis is graphically displayed in Figs. 5 and 6.

With regard to vertical deformations, as it can be seen in Fig. 7, this hypothesis entails that the larger vertical

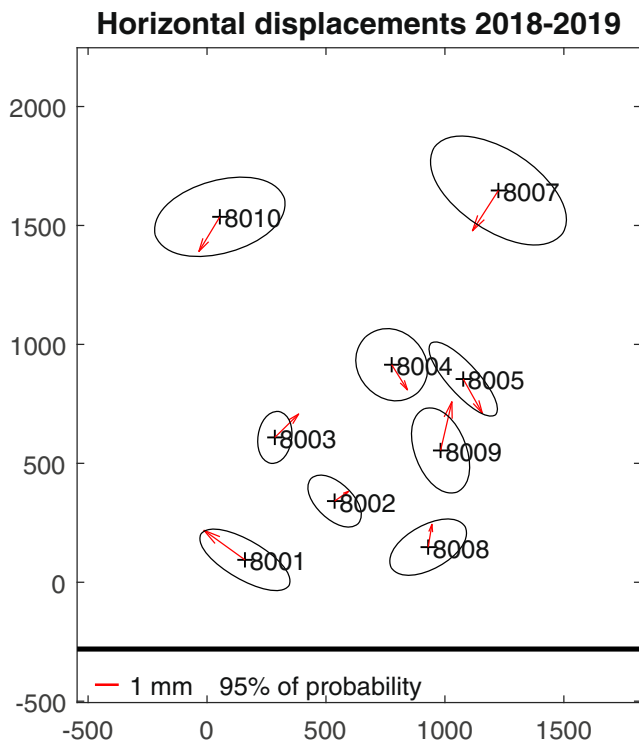


Fig. 5 Horizontal displacements obtained from 2018 to 2019 under the hypothesis that all points are stable

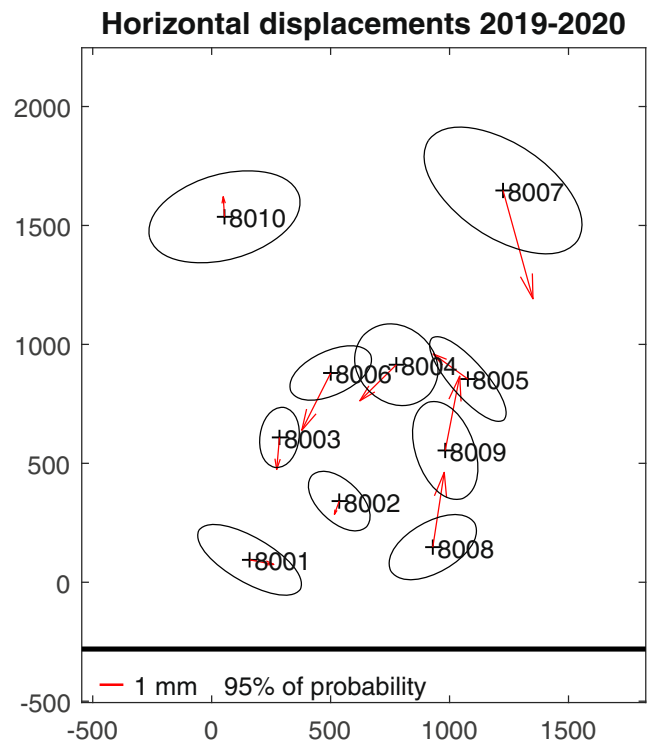


Fig. 6 Horizontal displacements obtained from 2019 to 2020 under the hypothesis that all points are stable

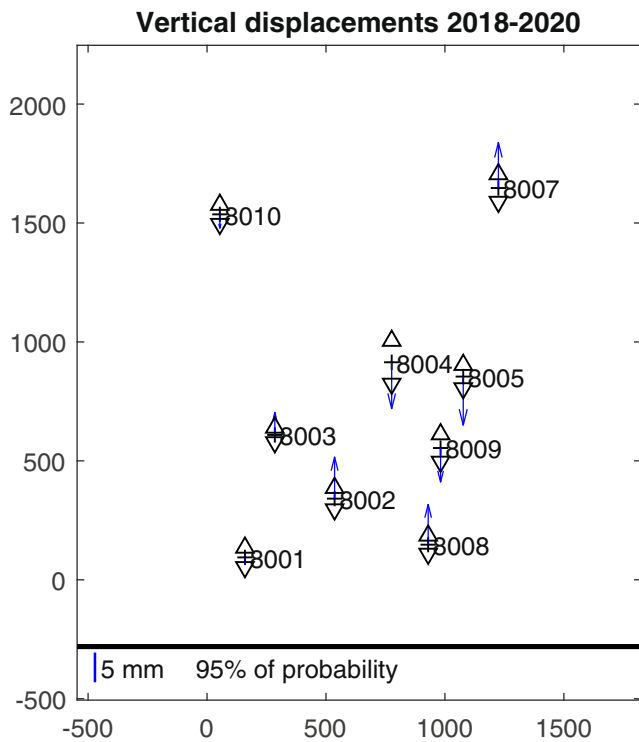


Fig. 7 Vertical displacements obtained from 2018 to 2020 under the hypothesis that all points are stable

displacements appear to be equally distributed upwards and downwards, which is mathematically valid but difficult to explain from a dynamical point of view.

Solution adopted as optimal

Considering that all the hypotheses tested resulted in that most of the network points had displaced a few millimeters between the years 2018 and 2020, the underlying assumptions for the solution eventually adopted as optimal were a balanced mix of those previous results and the following technical decisions.

Firstly, we considered that the datum selection should be only based on those points that are to be subsequently used as stations to provide coordinates of check points on the rocky wall or ground control for TDP or TLS. Therefore, points No. 8007 and No. 8010 were excluded from the congruency test.

Secondly, given that none of the 3D congruency tests succeeded in finding a stable set of points, the datum selection would be specified separately for horizontal and vertical components. Consequently, the deformation analysis was also split into 2D and 1D congruency tests.

Thirdly, the criterion followed to determine the optimal datum for deformation analysis was different for horizontal and vertical components. For horizontal components, we

Table 4 Results of the congruency test for the complete network by applying 2D conventional deformation analysis

Years	$\hat{\sigma}_0^2$	q_Δ	f	h	F_d	$F_{0.95,h,f}$	Def
18–19	0.896	127.04	13	21	10.12	2.55	Yes
19–20	1.138	198.16	16	24	12.43	2.37	Yes
18–20	0.842	567.77	13	21	48.14	2.55	Yes

Table 5 Results of the congruency test by applying a point-by-point 2D conventional deformation analysis

Point	dx (mm)	dy (mm)	F_d	$F_{0.95,h,f}$	Def
8001	-1.13 ± 0.58	1.08 ± 0.36	3.96	3.81	Yes
8002	-0.35 ± 0.39	-0.77 ± 0.36	4.55	3.81	Yes
8003	1.24 ± 0.27	-0.54 ± 0.26	11.21	3.81	Yes
8004	-0.64 ± 0.26	-3.67 ± 0.53	20.69	3.81	Yes
8005	-0.05 ± 0.34	-2.21 ± 0.42	28.23	3.81	Yes
8008	0.42 ± 0.54	2.46 ± 0.44	16.23	3.81	Yes
8009	0.50 ± 0.42	3.66 ± 0.55	22.55	3.81	Yes

Fig. 8 2018–2020 horizontal displacements obtained under the hypothesis adopted as optimal

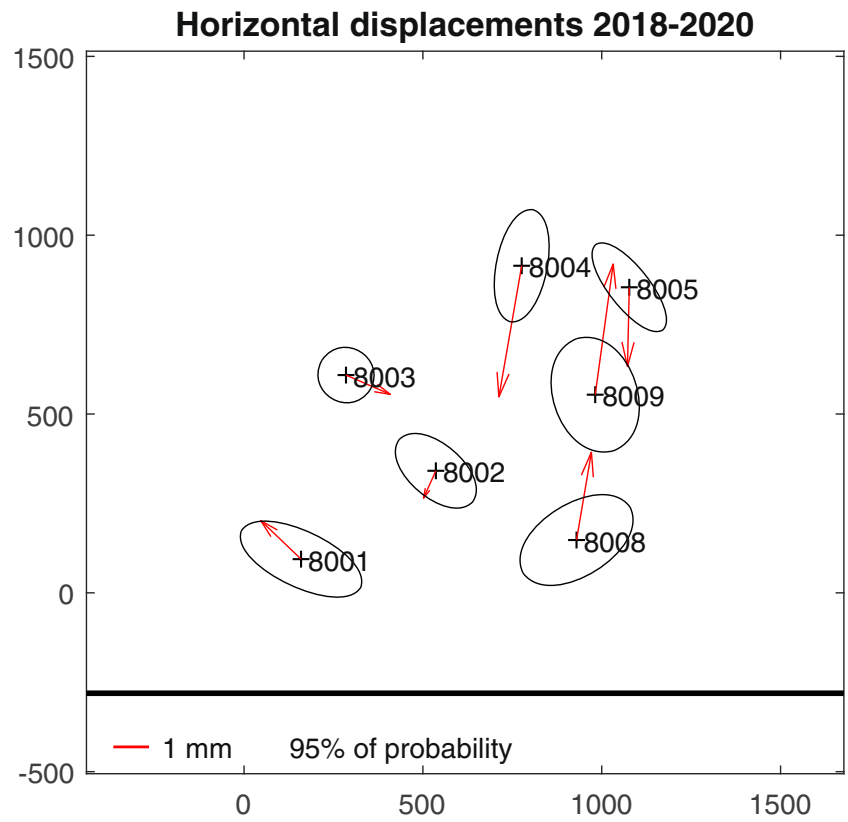


Fig. 9 Vertical displacements obtained from 2018 to 2020 under the hypothesis adopted as optimal

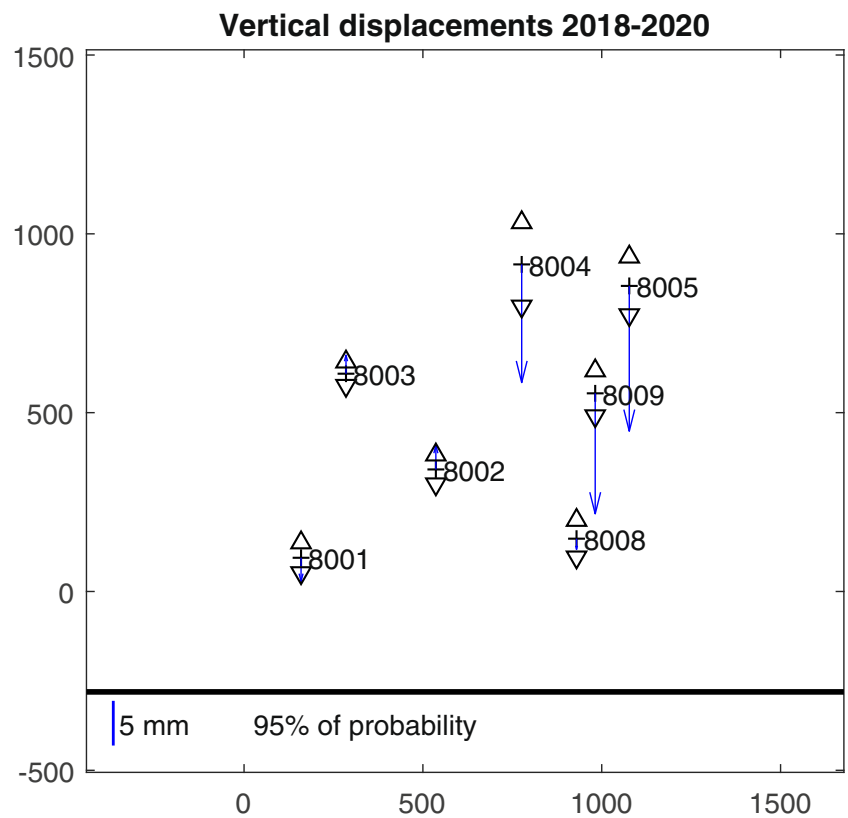


Table 6 Results of the congruency test for the complete network by applying 1D conventional deformation analysis

Years	$\hat{\sigma}_0^2$	q_Δ	f	h	F_d	$F_{0.95,h,f}$	Def
18–19	0.896	8.65	13	21	1.68	2.91	No
19–20	1.138	11.15	16	24	1.63	2.74	No
18–20	0.842	10.61	13	21	2.10	2.91	No

opted for those points that favored a no-net-rotation condition for the 2D deformations, while the minimization of upwards displacements was the condition selected for vertical deformations.

Since the adjustment results for each individual campaign obtained under this hypothesis were like those obtained under the initial hypothesis, only the results concerning 2D and 1D congruency tests are given in what follows.

Regarding horizontal deformations, the CDA results confirmed that all points had significant displacements from 2018 to 2020, but only those points in the vicinity of the water reservoir reached 2D displacements around 2–3 mm (Tables 4 and 5). Moreover, points No. 8004 and No. 8005, which are in the southern shoreline, seem to be approaching points No. 8008 and No. 8009, which are placed in the northern one (Fig. 8).

Concerning vertical deformations, the decision of excluding those points seemingly sinking around the water reservoir (No. 8004, No. 8005, No. 8008, and No. 8009) proved to be valid for the definition of a stable vertical datum where significant downwards displacements can be clearly identified (Fig. 9). The subsequent single point 1D analysis showed that all points defining the vertical datum can be considered stable from 2018 to 2020 (Tables 6 and 7).

In this solution, the vertical displacement of points No. 8004, No. 8005, and No. 8009 are $-13.22 \text{ mm} \pm 4.38 \text{ mm}$, $-16.25 \text{ mm} \pm 3.08 \text{ mm}$, and $-13.48 \text{ mm} \pm 2.40 \text{ mm}$, respectively.

Conclusions

In the light of our experience in Cortes de Pallás, some conclusions can be drawn. First, geodetic techniques, and specifically sub-millimetric EDM based ones, can provide coordinates with a precision better than 1 ppm even at distances larger than 1 km. Therefore, the establishment of well-controlled reference frames in critical deformation monitoring projects is not only possible, but also mandatory. Otherwise, long-term monitoring projects based on periodical campaigns by using traditional surveying or remote sensing techniques cannot be consistently integrated in a unique datum and thus, the deformation diagnosis derived from them will be consequently biased.

Second, when sub-millimetric geodetic techniques are used, especially in areas with apparent geotechnical problems like the current case in Cortes de Pallás, the comforting hypothesis of having stable points to serve as reference frame is no longer valid because small horizontal displacements of only several millimeters can be significantly detected in a short period of time with the mere use of the conventional deformation analysis. Consequently, the question of finding a stable datum becomes mathematically problematic and no clear procedure can be found in literature. In this case, we opted for a solution suitable to the reference frame practical purpose, although it is clear that it is a matter of time that the approximate coordinates obtained in 2018 do not fulfil the requisites for conventional deformation analysis and new proposals should be investigated.

Table 7 Results of the congruency test by applying a point-by-point 1D conventional deformation analysis

Point	dx (mm)	dy (mm)	F_d	$F_{0.95,h,f}$	Def
8001	-1.13 ± 0.58	1.08 ± 0.36	3.96	3.81	Yes
8002	-0.35 ± 0.39	-0.77 ± 0.36	4.55	3.81	Yes
8003	1.24 ± 0.27	-0.54 ± 0.26	11.21	3.81	Yes
8004	-0.64 ± 0.26	-3.67 ± 0.53	20.69	3.81	Yes
8005	-0.05 ± 0.34	-2.21 ± 0.42	28.23	3.81	Yes
8008	0.42 ± 0.54	2.46 ± 0.44	16.23	3.81	Yes
8009	0.50 ± 0.42	3.66 ± 0.55	22.55	3.81	Yes

Third, although it is commonly admitted that traditional surveys based on total stations or 3D point clouds derived from remote sensing techniques are reasonably well integrated by using GNSS techniques, our experience demonstrates that monitoring of high-precision reference frames requires state-of-the-art geodetic instruments, like long-range sub-millimetric EDMs, as well as length metrology methods.

Funding Open Access funding provided thanks to the CRUE-CSIC agreement with Springer Nature.

Acknowledgements This work has been carried out under the contract T-726 – *Control de deformaciones en la ladera norte de la muela de Cortes de Pallás* commissioned by the *Diputació de València*. The authors are grateful to the UCM which granted the use of its ME5000 Mekometer through a co-operation agreement, to José María Grima for his support to calibrate the ME5000 Mekometer, thermometers, and barometers at the Calibration Laboratory of the UPV. We also acknowledge IGS for their efforts to disseminate products available to the global community, and EURAMET for their contribution to the research efforts on the field of large-scale length metrology for geodesy. The UPV team acknowledge the *Programa de Ayudas de Investigación y Desarrollo (PAID-01-20) de la Universitat Politècnica de València* for funding the research contract of Raquel Luján

Declarations

Conflict of interest The authors declare no competing interests.

Open Access This article is licensed under a Creative Commons Attribution 4.0 International License, which permits use, sharing, adaptation, distribution and reproduction in any medium or format, as long as you give appropriate credit to the original author(s) and the source, provide a link to the Creative Commons licence, and indicate if changes were made. The images or other third party material in this article are included in the article's Creative Commons licence, unless indicated otherwise in a credit line to the material. If material is not included in the article's Creative Commons licence and your intended use is not permitted by statutory regulation or exceeds the permitted use, you will need to obtain permission directly from the copyright holder. To view a copy of this licence, visit <http://creativecommons.org/licenses/by/4.0/>.

References

- Baselga S, García-Asenjo L, Garrigues P (2014) Practical formulas for the refraction coefficient. *J Surv Eng* 140(2):06014,001. [https://doi.org/10.1061/\(ASCE\)SU.1943-5428.0000124](https://doi.org/10.1061/(ASCE)SU.1943-5428.0000124)
- Bell B (1992) Workshop on the use and calibration of the kern me5000 mekometer. In: Proc. Stanford Linear Accelerator Center, Stanford University, USA, 18-19 June, p 1–80
- Blažič G (1982) Free networks : minimum norm solution as obtained by the inner adjustment constraint method. *Bull Géod* (56)209–219
- Caspary WF (1987) Concepts of network and deformation analysis. In: Monograph 11. The University of New South Wales, Australia, pp 593–66
- Chen YG, Chrzanowski A, Secord J (1990) A strategy for the analysis of the stability of reference points in deformation surveys. *CISM J ACSGG* 44(2):141–149
- Chen YQ (1983) Analysis of deformation surveys—a generalized method. Technical Report No 94 University of New Brunswick, Fredericton, pp 54–72
- Ciddor PE (1996) Refractive index of air: new equations for the visible and near infrared. *Appl Opt* 35(9):1566–1573. <https://doi.org/10.1364/AO.35.001566>
- Ciddor PE (2002) Refractive index of air: 3. the roles of co₂, h₂o, and refractivity virials. *Appl Opt* 41(12):2292–2298. <https://doi.org/10.1364/AO.41.002292>
- Ciddor PE, Hill RJ (1999) Refractive index of air. 2. group index. *Appl Opt* 38(9):1663–1667. <https://doi.org/10.1364/AO.38.001663>
- Di Stefano F, Cabrelles M, García-Asenjo L et al (2020) Evaluation of long-range mobile mapping system (MMS) and close-range photogrammetry for deformation monitoring. A case study of Cortes de pallás in Valencia (Spain). *Appl Sci*, 10(19). <https://doi.org/10.3390/app10196831>
- Dodson AH, Zaher M (1985) Refraction effects on vertical angle measurements. *Surv Rev* 28(217):169–183. <https://doi.org/10.1179/sre.1985.28.217.169>
- Francioni M, Salvini R, Stead D et al (2018) Improvements in the integration of remote sensing and rock slope modelling. *Nat Hazards* 90(2):975–1004. <https://doi.org/10.1007/s11069-017-3116-8>
- García-Asenjo L, Baselga S, Garrigues P (2017) Deformation monitoring of the submillimetric upv calibration baseline. *Journal of Applied Geodesy* 11(2):107–114. <https://doi.org/10.1515/jag-2016-0018>
- García-Asenjo L, Martínez L, Baselga S et al (2019) Establishment of a multi-purpose 3D geodetic reference frame for deformation monitoring in Cortes de Pallás (Spain). In: Proc. 4th Joint International Symposium on Deformation Monitoring (JISDM) 15-17 May 2019, Athens, Greece
- Grafarend E, Sansò F (eds) (1985) Optimization and design of geodetic networks. Springer-Verlag, Berlin
- Harmening C, Neuner H (2019) Evaluating the performance of a space-and time-continuous deformation model. In: Proc. 4th Joint International Symposium on Deformation Monitoring (JISDM) 15-17 May 2019, Athens, Greece
- IUGG (1999) Resolutions adopted at the XXII general assembly by the International Union of Geodesy and Geophysics (IUGG) Associations. In: Proc., Univ. of Birmingham, Birmingham, U.K., 110–111
- Jokela J, Häkli P (2010) Interference measurements of the Nummela Standard Baseline in 2005 and 2007. Publications of the Finnish Geodetic Institute. No. 144
- Klein I, Matsuoka MT, GM P et al (2019) A new relationship between the quality criteria for geodetic networks. *J Geod* 93(217):529–544
- Lehman R, Lösler M (2016) Multiple outlier detection: hypothesis tests versus model selection by information criteria. *J Surv Eng* 124(4):04016,017. <https://doi.org/10.1061/%28ASCE%29SU.1943-5428.0000189>
- Niemeier W (1981) Statistical tests for detecting movements in repeatedly measured geodetic networks. *Tectonophysics* 71:335–351. <https://doi.org/10.1016/B978-0-444-41953-8.50041-4>
- Niemeier W, Velsink H (2019) Strategies and methods for multi-epoch deformation analysis based on geodetic networks. In: Proc. 4th Joint International Symposium on Deformation Monitoring (JISDM) 15-17 May 2019, Athens, Greece
- Nowel K (2019) Squared Msplit(q) S-transformation of control network deformations. *J Geod* 93:1025–1044. <https://doi.org/10.1007/s00190-018-1221-4>

- Pollinger F (2020) Refractive index of air. 2. group index: comment. *Appl Opt* 59(31):9771–9772. <https://doi.org/10.1364/AO.400796>
- Pollinger F, Courde C, Eschelbach C et al (2021) Large-scale dimensional metrology for geodesy—first results from the European GeoMetre Project. Springer, Berlin, pp 1–6. https://doi.org/10.1007/1345_2022_168
- Rüeger JM (ed) (1996) Electronic distance measurement. Springer-Verlag, Berlin
- Velsink H (2015) On the deformation analysis of point fields. *J Geod* 89(11):1071–1087. <https://doi.org/10.1007/s00190-015-0835-z>
- Wiśniewski Z, Zienkiewicz M (2016) Shift-msplit* estimation in deformation analysis. *J Surv Eng* 142(4):04016,015. [https://doi.org/10.1061/\(ASCE\)SU.1943-5428.0000183](https://doi.org/10.1061/(ASCE)SU.1943-5428.0000183)

Publisher's Note Springer Nature remains neutral with regard to jurisdictional claims in published maps and institutional affiliations.

Affiliations

Luis García-Asenjo¹  · Laura Martínez² · Sergio Baselga¹ · Pascual Garrigues¹ · Raquel Luján¹

Laura Martínez
laura.martinez@dival.es

Sergio Baselga
serbamo@cgf.upv.es

Pascual Garrigues
pasgarta@cgf.upv.es

Raquel Luján
ralugar@cgf.upv.es

¹ Department of Cartographic Engineering, Geodesy and Photogrammetry, Universitat Politècnica de València, Camino de Vera s/n, Valencia, 46022, Spain

² Department of Roads and Infrastructures, Diputació de València, c/ Hugo de Moncada, 9, Valencia, 46010, Spain